Spatial and Temporal Resolution of Luminescence Quenching in Small Upconversion Nanocrystals

Federico Pini, Laura Francés-Soriano, Nicola Peruffo, Antonio Barbon, Niko Hildebrandt, Marta Maria Natile

Spatial and temporal resolution of luminescence quenching in small upconversion nanocrystals

Federico Pini,[1,2,3] Laura Francés-Soriano,[1] Nicola Peruffo,[2,3] Antonio Barbon,[3] Niko Hildebrandt,[1,4,5] and Marta Maria Natile*[2,3]*

[1] nanofret.com, Laboratoire COBRA, Université de Rouen Normandie, CNRS, INSA, 76821 Mont-Saint-Aignan Cedex, France.

[2] Istituto di Chimica della Materia Condensata e Tecnologie dell'Energia (ICMATE), Consiglio Nazionale delle Ricerche (CNR), Via F. Marzolo 1, 35131 Padova PD, Italy.

[3] Dipartimento di Scienze Chimiche, Università di Padova, Via F. Marzolo 1, 35131 Padova PD, Italy.

[4] Department of Chemistry, Seoul National University, Seoul 08826, South Korea.

[5] Université Paris-Saclay, 91405 Orsay Cedex, France.

*e-mail: niko.hildebrandt@univ-rouen.fr; martamaria.natile@unipd.it

Abstract. Luminescent upconversion nanocrystals (UCNCs) have become one of the most promising nanomaterials for biosensing, imaging, and theranostics. However, their ultimate translation into robust luminescent probes for daily use in biological and medical laboratories requires comprehension and control of the many possible deactivation pathways that cause upconversion luminescence (UCL) quenching. Here, we demonstrate that thorough modelling of UCL rise and decay kinetics using a freely accessible software can identify the UCL quenching mechanisms in small (<40 nm) UCNCs with spatial and temporal resolution. Applied to the most relevant β-$NaYF_4$:Yb^{3+},Er^{3+} UCNCs, our model could show that only few distinct non-radiative low-energy transitions were deactivated via specific solvent and ligand vibrations with a strong downstream effect on the population and depopulation dynamics of the emitting states. UCL quenching could penetrate circa 4 nm inside the UCNC, which resulted in significant size-dependent changes of UCL intensities and spectra. Despite the large surface-to-volume ratios and UCL quenching via the UCNC surface, we found strong contributions of the outer layers to the overall UCL, which will be highly important for the design of UCNPs to investigate biomolecular interactions via distance-dependent energy transfer methods. Our advanced kinetic model is easily scalable to different UCNC architectures, environments, and energy transfer interactions, such that relatively simple modelling of UCL kinetics can be used for efficiently optimizing UCNCs for their final application as practical luminescent probes.

Keywords: *upconversion, energy migration, nanoparticles, luminescence, kinetic modelling*

Introduction

Rare earth (RE)-based upconversion (or upconverting) nanocrystals (UCNCs) can produce narrow luminescence bands over a broad spectral range (usually in the ultraviolet (UV), visible (VIS) and near infrared (NIR)) via the sequential absorption of NIR photons.[1–5] Their emission color can be easily modified by changing the RE dopants and they possess chemical and colloidal stability and low toxicity.[6] These unique optical features have made UCNCs very special nanotools for biosensing,[7,8] photothermal and photoactivated therapy,[9,10] bioimaging,[11] or optical thermometry.[12] Although these applications have demonstrated the huge potential of these NCs, the complete comprehension of their properties requires more fundamental studies. The photophysics of UCNCs is highly complicated, including many radiative and non-radiative energy transitions or pathways, such as cross-relaxation (CR), energy migration, and phonon coupling within the UCNC and energy transfer (ET) to the UCNC-surrounding environment.[13] The sophisticated dynamics of UCNCs strongly influence their UC luminescence (UCL) both spectrally (*i.e.*, varying intensities of the different emissive transitions, such as the red/green intensity ratios of Er^{3+}-doped UCNCs) and temporally (*i.e.*, multiexponential kinetics with varying rise and decay times). A more comprehensive understanding of the UC dynamics and the pathways involved in the quenching phenomena at the nanoscale is essential for a rational design of UCNCs with improved luminescence efficiencies.[14–16]

More and more attention has been devoted to model the optical properties of these materials and two main approaches have been applied: density functional theory (DFT) and classical kinetic methods. Seminal DFT studies have evidenced the relation between the NC structure, stability, RE distribution, surface defects, ligand coverage, and the UCL.[17] Kinetic models have been based on the resolution of differential rate equations with the aim to describe the population dynamics, *i.e.*, the specific paths of the population and depopulation of the energy states in RE ions.[15,18–20] UCL in UCNCs is a rather complex process, comprising direct population of states, energy exchange between states, and energy depopulation processes. Simplified kinetic models that consider only the decay processes are most often used because the differential equations can be analytically solved as multiexponential curves.[19,21] Berry *et al.* introduced a detailed kinetic model that considered the non-emitting states and all the main ET processes between the RE ions to account for indirect population and depopulation processes.[22] However, this model did not consider the inhomogeneity of UCNCs, *i.e.*, the different quenching behaviors in the internal core and the outer layers close to the surface. Kinetic modelling has been mainly used to investigate the UCL-dependence on power density[21–26] and RE ion doping concentration.[17,27,28] In an approach combining a microscopic random walk with rate equations, Chan *et al.* were able to include

more than 30 electronic states in their model to provide a detailed analysis of the population dynamics in UCNCs under a wide range of power densities.[15] Considering that it is well accepted that the interaction of the activator and sensitizer RE ions with the capping ligands and solvent molecules via energy-resonance with their vibrational frequency overtones is one of the major causes of UCL quenching,[25,29] it is almost surprising that only few studies investigated the surface or solvent quenching and the effect of crystal size by kinetic modelling.[19,29,30] Clearly, the different approaches and results discussed above show that the quenching pathways of UCNCs have not been fully understood and that further advances are necessary to provide deeper insights into the complicated energy pathway networks.

In this work, we analyze the optical properties of several β-$NaYF_4$:Yb^{3+},Er^{3+} UCNCs of different sizes upon pulsed NIR excitation by means of a kinetic model that can discriminate the processes most affected by the environmental conditions and NC size and spatially resolve the luminescence quenching dynamics. Our kinetic model, developed on a freely accessible modelling software (COPASI),[31] considers all types of processes, including photon absorption, self-absorption, ET, UC, CR, and radiative and non-radiative relaxations among RE ions. It is also able to reproduce the time evolution (both UCL rise and decay) of the different wavelength emissions of UCNCs. Studying the green and red Er^{3+} UCL, we observed an increase of only a small number of non-radiative kinetic constants for all UCNC sizes, suggesting a solvent specific effect due to the coupling with vibrational modes. Involvement of specific vibrational modes was demonstrated by the use of different and isotopically substituted solvents. As expected, quenching was stronger for smaller UCNCs due to the larger surface-to-volume ratios. The spatial resolution of our model, which considers an inner core and an outer "solvent-interacting" layer as well as their inter-compartment interactions, allowed us to determine the penetration depth of the surface quenching. Our complete modelling approach can provide important details of UCL processes, which are important not only for a better fundamental knowledge but also for an optimized design of UCNC architectures toward advanced applications.

Results and Discussion

Upconversion nanocrystals (UCNCs). To verify the applicability of our model to describe the photophysics of UCNCs and rationalize the influence of NC size and solvents in UCL quenching, we investigated typical oleate-capped hexagonal phase (β) $NaYF_4$ NCs containing 20% of Yb^{3+} (sensitizer) and 2% of Er^{3+} (activator). Three core UCNCs (c-UCNCs) with diameters of 27±2 nm, 31±2 nm, and 39±4 nm were synthesized. As reference material, core-shell UCNCs (cs-UCNCs) of 38±2 nm in diameter, consisting of a core of 30±2 nm and an inert shell (pure β-$NaYF_4$) of ~4 nm, were prepared by

a layer-by-layer method employing sacrificial nanocrystals of ~6 nm (**Supporting Figure S1**) as the shell precursor material.[7] A shell thickness of 4 nm was selected because it was found to effectively suppress UCL quenching.[30,32] Transmission electron microscopy (TEM) images, powder X-ray diffraction (PXRD) patterns, and steady-state UCL spectra of the UCNCs are shown in **Figure 1**. All UCNCs were monodisperse in size and with hexagonal phase. DRIFT spectra confirmed the oleate capping (**Supporting Figure S2**). The emission spectra display the typical multiple emission bands of Er^{3+} 4f-4f transitions at 410 nm (blue emission, $^2H_{9/2} \rightarrow {}^4I_{15/2}$), 520 nm and 540 nm (green emission, $^2H_{11/2} \rightarrow {}^4I_{15/2}$ and $^4S_{3/2} \rightarrow {}^4I_{15/2}$), and 660 nm (red emission, $^4F_{9/2} \rightarrow {}^4I_{15/2}$) (**Figure 1c** for UCNCs dispersed in toluene and **Supporting Figure S3** for UCNCs dispersed in cyclohexane and deuterated toluene, respectively). As expected, due to the larger amounts of RE ions in larger NCs, the UCL intensities increased with increasing UCNC sizes. The addition of an inert shell (to minimize the surface quenching) resulted in a significant enhancement of the UCL intensity (~6-fold that of c-UCNCs in toluene).

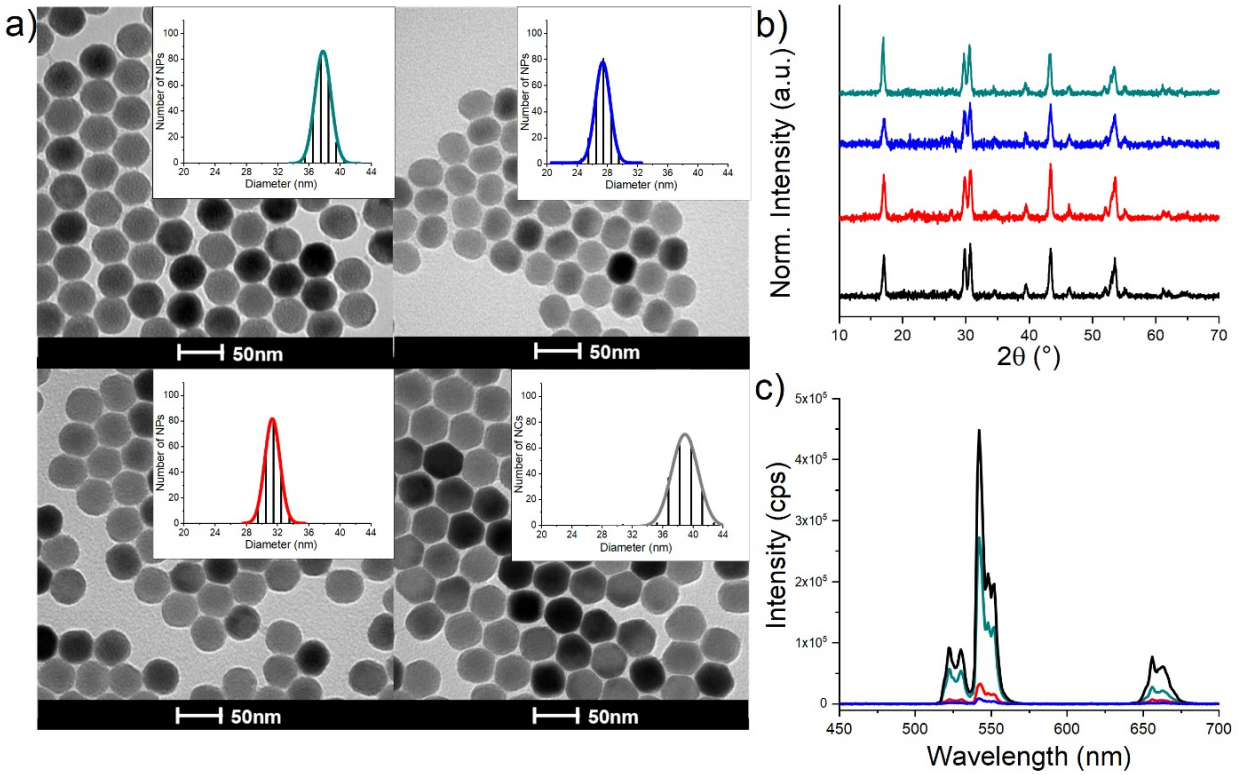

Figure 1. a) TEM images and histogram of crystal-size distributions of cs-UCNCs (30±2 nm active core with 4 nm inert shell, green line) and c-UCNCs (27±2 nm (blue line); 31±2 nm (red line); 39±4 nm (black line)). **b)** PXRD diffraction patterns of the different UCNCs. **c)** UCL spectra of the same UCNCs dispersed in toluene (5 mg/mL) under 980 nm excitation at 1.30 W cm^{-2} (the weak blue emission around 410 nm is not shown).

Solvent-and-size-dependent UCL quenching. The UCL dynamics of the green and red emission of the Er^{3+}-doped UCNCs were thoroughly investigated by modelling the time-resolved UCL measured for all UCNCs dispersed in three different non-polar solvents, namely toluene, deuterated toluene, and cyclohexane (concentration of dispersions: 1 mg/mL). The oleate-capped UCNCs formed stable dispersions in all three solvents, which allowed us to consider the quenching contribution of the oleates as constant and directly compare the quenching contributions of the different solvents. First, a *single-compartment* kinetic model (details are reported in the Material and Methods section and in the Supporting Information), considering all elementary photophysical processes involved in UCL (**Figure 2**), was considered to model the time-resolved green and red UCL. It is well recognized that the green UCL can be attained primarily in a two-step ET (*1Er* → *3Er* → *7Er*) followed by NR relaxation *7Er* → *6Er*.[20,33] The red UCL is more disputed, and the main pathway strongly depends on the excitation power density.[29,33] Our model accounts for all the proposed pathways.

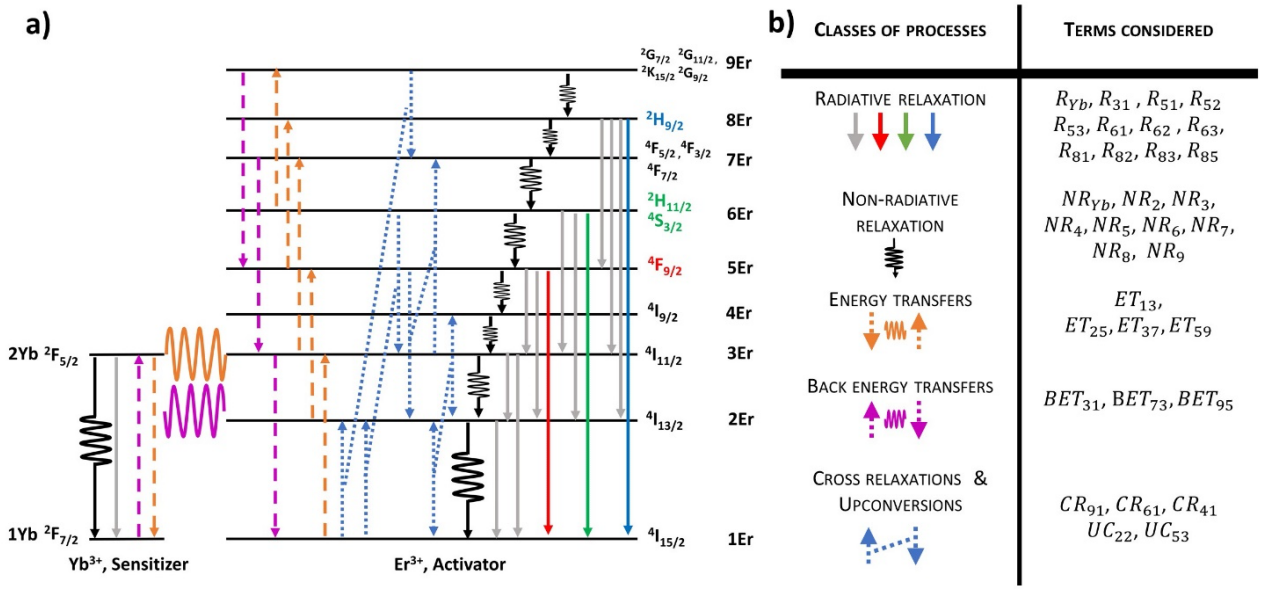

Figure 2. a) Schematic diagram illustrating the most important processes relevant to UCL of UCNCs. The UCL emission involves absorbance of excitation light by Yb^{3+}, followed by successive ET events to Er^{3+}. Dashed orange arrows indicate $Yb^{3+} \rightarrow Er^{3+}$ ET; the purple dashed arrows indicate back ET (BET) from Er^{3+} to Yb^{3+}. Paired dotted blue arrows indicate CR and UC processes within Er^{3+} ions. Black zigzag arrows indicate non-radiative relaxations (NR). Solid arrows indicate radiative relaxations (R), corresponding to blue, green, and red UCL and NIR emission. **b)** Types of processes and the respective terms considered in the kinetic model. Some of the spectroscopic terms are grouped on the base of similar energies.[22]

The green and red UCL kinetics of the reference cs-UCNCs dispersed in toluene were modeled starting from the kinetic-parameter values optimized by Berry *et al.* for a polycrystalline powder[20,22] by using 11 differential equations (see Supporting Information for details) describing the rate of change in

the population density for each electronic state of Er^{3+} and Yb^{3+}. The initial populations of the electronic states of Yb^{3+} and Er^{3+} ions were calculated considering that only the *1Er*, *3Er*, *1Yb*, and *2Yb* states (**Figure 2a**) can be directly populated by the 980 nm NIR pulse (power density of 12.3 mW/cm^2) and based on UCNC concentration, RE doping, and absorbance of the dispersion. The green and red UCL datasets were modelled simultaneously to ensure the same weight for both processes. Unlike Berry *et al.*,[22] who fitted only a selected number of constants, our model optimized all kinetic constants concurrently and no ancillary boundary conditions were applied. The kinetic parameters obtained for the cs-UCNCs in toluene were used as starting values for modelling the time-resolved UCL of the three c-UCNCs in the three different solvents. **Figure 3** shows the very good agreement between the experimental and simulated time-resolved green (λ_G = 542±10 nm) and red (λ_R = 660±7 nm) UCL for all the c-UCNCs after pulsed excitation at 980 nm (61 μJ/cm^2/pulse). Time-resolved green and red emission of cs-UCNCs in the three solvents are shown in **Supporting Figure S4**. The corresponding kinetic constants are listed in **Supporting Tables S1 to S3**. The simulations revealed that changing UCNC size and/or the solvent affected only a restricted number of kinetic constants that are all non-radiative, which suggests that they account for specific quenching processes. In particular, for all the investigated c-UCNCs only the non-radiative constants k_{Yb_NR}, k_{NR2}, k_{NR3}, and k_{NR5} changed significantly (between ~160 % and ~64000 %) compared to cs-UCNCs, whereas all other constants changed less than 100 % (in the large majority of cases less than 20 %).

The specific quenching can be explained considering the physical meaning of these parameters. The non-radiative terms include all those processes that are different from ET or CR. Thus, k_{NRj} can be deconvoluted in two terms, one deriving from the coupling of the electronic transition with multi-phonon relaxations (k_{MPR}) and the other originating from the coupling with solvent vibrational modes (k_{isolv}). The general expression for the non-radiative depopulation term of an erbium electronic state is then:

$$\left(\frac{\partial n_{iEr}}{\partial t}\right)_{NR} = -k_{NRi} n_{iEr} = -(k_{MPR} + k_{isolv} n_{solv}) n_{iEr} \qquad (1),$$

where n_{solv} represents the solvent population. The solvent population is much larger than the ion population and can be approximated as constant. Decreasing the size of the UCNCs will result in a strong increase of k_{isolv} because a larger number of ions will interact with the solvent and consequently in an increase of k_{NRi}. Changing the solvent should also influence the radiative kinetic constants, which were reported by Rabouw *et al.* as follows:[19,34,35]

$$k_R(n) = k_R^{bulk} \cdot x = \frac{k_R^{bulk}}{\mu}\left(\frac{3\mu^2}{2\mu^2+\mu_{NC}^2}\right)^2 \qquad (2),$$

where k_R^{bulk} is the bulk radiative kinetic constant and μ and μ_{NC} are the refractive indices of the solvent and the UCNC, respectively. With μ_{NC}=1.475,[36] μ_{tol}=1.498, μ_{cyclo}=1.427 and μ_{tolD}=1.494, the multiplicative factors in Equation 2 result in $x = 0.678$, $x = 0.666$, and $x = 0.677$ for toluene, cyclohexane, and deuterated toluene, respectively. Thus, the differences in the resulting radiative kinetic constants in those solvents are below 2 %, which explains why the model does not find any significant differences either.

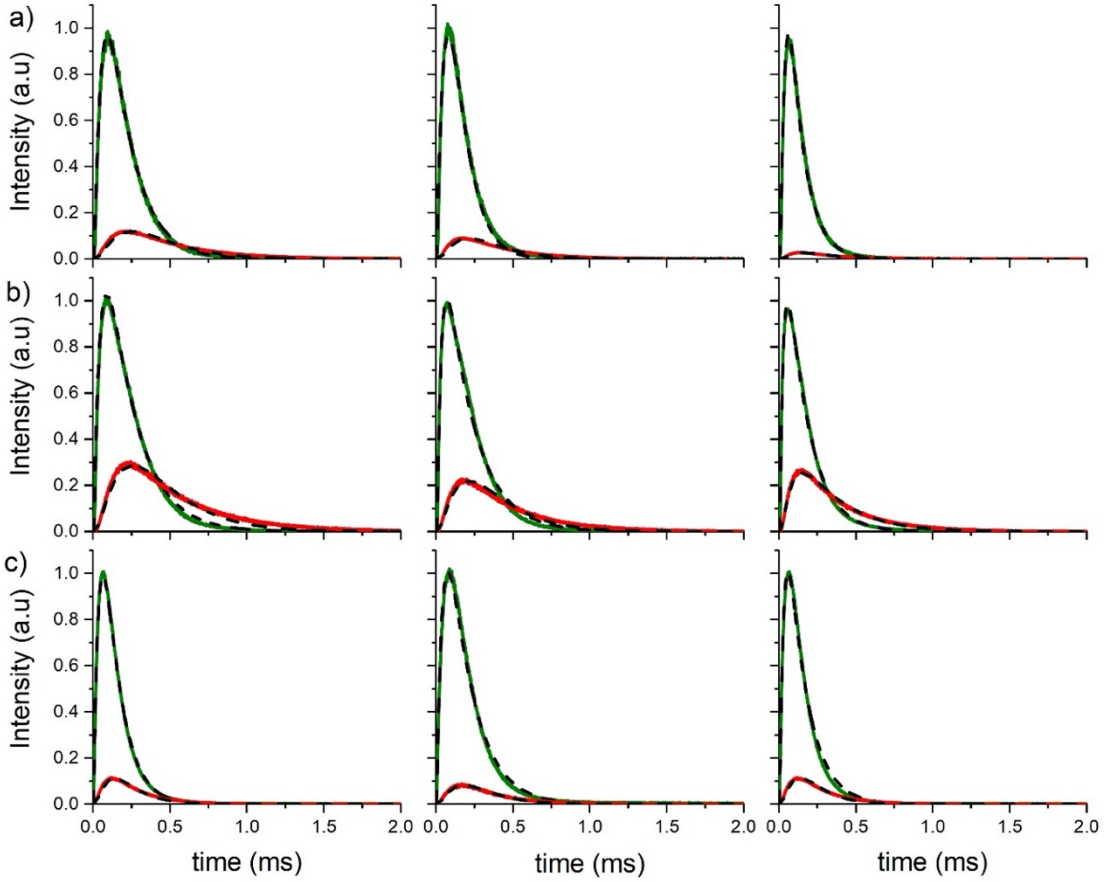

Figure 3. Experimental (green and red solid lines) and simulated (black dashed lines) time-resolved green and red emission for all the c-UCNCs (39 nm, 31 nm, and 27 nm from left to right) dispersed in toluene (**a**), cyclohexane (**b**), and deuterated toluene (**c**) following 980 nm pulsed excitation (~ 61 μJ cm^{-2}). Emission intensity was normalized to the highest intensity value (green emission).

A detailed analysis of the data collected in toluene showed that only k_{YbNR}, k_{NR2}, and k_{NR3} increased significantly (see **Supporting Table S1** for all kinetic constants) compared to the reference values of the cs-UCNCs. It is noteworthy that none of these kinetic constants is directly related to the emitting *5Er* (red) or *6Er* (green) states. The trend of these kinetic constants *versus* the UCNC sizes (**Figure 4a**) highlights the stronger quenching with decreasing NC size. This behavior was not unexpected because the surface-to-volume ratio increases with decreasing NC size and thus, the UCNC-

solvent interaction becomes more important. Although the increase was observed for all three non-radiative constants, it is evident that the relative increase (compared to the cs-UCNC reference system) is more pronounced for k_{NR2} (501, 565, and 599-fold for the 39 nm, 31 nm, and 27 nm c-UCNCs, respectively) and k_{NR3} (72, 102, and 153-fold for the 39 nm, 31 nm, and 27 nm c-UCNCs, respectively) than for k_{YbNR} (16, 21, and 22-fold for the 39 nm, 31 nm, and 27 nm c-UCNCs, respectively).

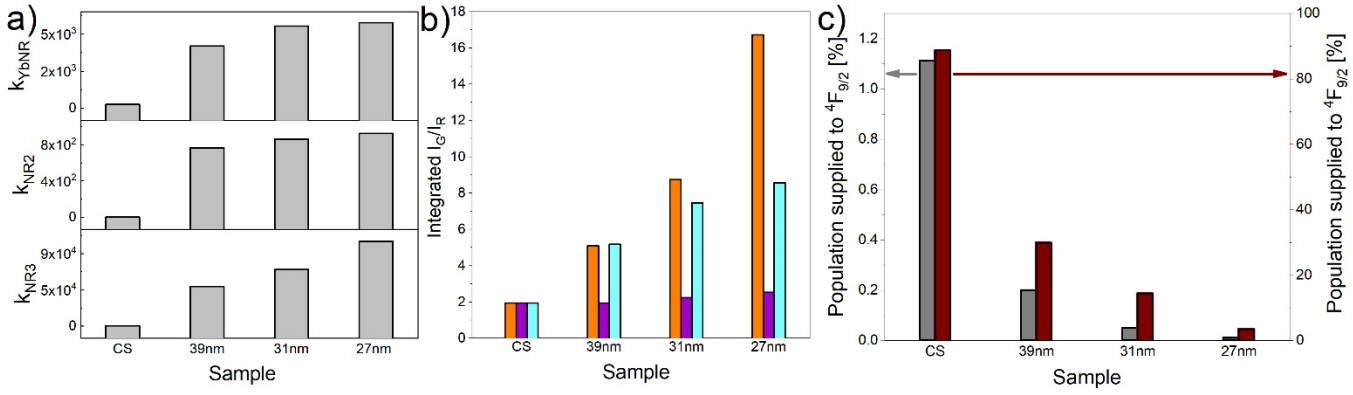

Figure 4. a) Calculated non-radiative kinetic constants of cs-UCNCs and c-UCNCs of different sizes dispersed in toluene. **b**) Green/red UCL intensity ratios of the same UCNCs dispersed in toluene (orange), deuterated toluene (magenta), and cyclohexane (cyan). **c)** Contribution to the population of *5Er* level of the same UCNCs dispersed in toluene: three-step path (grey) and two-step path (brown).

The information provided by the model via the three specific non-radiative kinetic constants allowed us to gain a better understanding of the UCL quenching mechanisms and the indirect influence on the different radiative transitions. For example, the quite different UCL quenching behaviors of red and green emission can be explained by the different energy pathways for populating the radiative states *5Er* (red) and *6Er* (green). The electronic state *6Er* is populated via two ETs from Yb ($2\times$ *2Yb* → *1Yb*) to Er (*1Er* → *3Er*, *3Er* → *7Er*) followed by a non-radiative relaxation to *6Er*. Thus, in principle *2Yb*, *3Er*, *7Er*, and *6Er* states would be prone to quenching. The *7Er* to *6Er* and *6Er* to *5Er* NR relaxations (which proceed via several intermediate states) via phonon coupling are more efficient than coupling to the vibrational overtones of toluene, which was confirmed by the stability of k_{NR7} and k_{NR6}. The *2Yb* and *3Er* states can be quenched by relaxation to the *1Yb* and *2Er* states via phonon-assisted coupling to the second (for *2Yb* → *1Yb*) and first (for *3Er* → *2Er*) vibrational frequency overtones of the aromatic =C–H stretching of toluene and subsequently the *2Er* state can be further quenched to the *1Er* ground state via phonon-assisted coupling to the fundamental vibrational frequency of the aromatic =C–H stretching of toluene (**Table 1**). This explains the strong increase of k_{Yb_NR}, k_{NR2}, and k_{NR3} in toluene. Thus, the green UCL is mainly quenched via those two excited states (*3Er* and *2Yb*). On the other hand, the *5Er* state can be populated via two main energy pathways. The first one is similar to the one for populating

6Er but contains an additional *6Er* → *5Er* relaxation via phonon coupling. In principle, the *5Er* state could be quenched by a relaxation to the *4Er* state, however, the energy difference (~2500 cm^{-1}) is too high for efficient phonon coupling and too low for coupling to the aromatic =C–H stretching of toluene (**Table 1**). This consideration is supported by the unchanged k_{NR5}. The difference in green and red UCL quenching must therefore be related to the second pathway for *5Er* population, which includes three ETs from Yb (3× *2Yb* → *1Yb*) to Er (*1Er* → *3Er*, *3Er* → *7Er, 6Er* → *9Er*) followed by BET from Er (*9Er* → *5Er*) to Yb (*1Yb* → *2Yb*). The quenching of *9Er* by the solvent is unlikely because the CR_{91} (*9Er* → *7Er*), the multiphonon coupling, and the BET are more efficient. All the other states involved in this *5Er* population pathway are also involved in the *6Er* population for green emission and therefore the most reasonable assumption is that the involvement of three ET steps (instead of two for green UCL) makes this pathway more prone to the depletion of *2Yb* and the lower Er states. The smaller the UCNC, the more important the interactions with the solvent, and the more significant the quenching of the second pathway for red emission, which leads to the size-dependent increase of the green/red ratio (**Figure 4b**). In other words, the smaller the UCNC the lower the relative contribution of the second (three ET steps) pathway to the population of *5Er* (**Figure 4c**).

Table 1. Non-radiative transitions affected by the solvent with respective energy gaps[37] and main quenching agents.[19,38–40]

Non-radiative transition	**Energy [cm^{-1}]**	**Vibrational & phonon coupling**
Yb^{3+}: $^2F_{5/2}$→ $^2F_{7/2}$ **[2Yb -> 1Yb]**	~10000	3 x =***C-H*** + 2 phonons
Er^{3+}: $^4I_{13/2}$-→ $^4I_{15/2}$ **[3Er -> 2Er]**	~6750	2 x =***C-H*** + 1 phonon 3x =***C-D***
Er^{3+}: $^4I_{11/2}$ → $^4I_{13/2}$ **[2Er -> 1Er]**	~3500	1 x =***C-H*** + 1 phonon
Er^{3+}: $^4F_{9/2}$→ $^4I_{11/2}$ **[5Er -> 4Er]**	~2500	1 x ***C-H*** - 1 phonon 1 x ***C-D*** + 1 phonon
Quenching Agent	**Energy dissipated [cm^{-1}]**	**Quenching mechanism**
Toluene	2900 - 3100	Aromatic =***C-H*** stretching
Cyclohexane	2750 - 3000	Aliphatic ***C-H*** stretching
Oleate	2800 - 3000	Aliphatic ***C-H*** stretching
Deuterated toluene	2250	Aromatic =***C-D*** stretching
$NaYF_4$	139, 161, 194, 261, 321, 398, 500	Phonon modes

To verify the hypothesized coupling of transitions from the lower energy levels with the vibrational frequencies (fundamental and overtones) of C-H stretching, the same time-resolved measurements and kinetic modelling were also carried out for c-UCNCs dispersed in deuterated toluene (**Figure 3b**). As expected, only a slight increase of the kinetic constants was observed (**Supporting Table S2**). Only k_{NR3} and k_{NR5} increased significantly (between 1.6 and 2-fold), although almost negligibly

when compared to the results observed in toluene (*vide supra*). The stronger implication of k_{NR5} in UCL quenching may be related to the lower energy of the =C–D stretching vibrational frequency: the fundamental better matches to the *5Er* → *4Er* transition and the second overtone to the *3Er* → *2Er* transition (**Table 1**). The overall small increase of the two non-radiative kinetic constants suggests a rather non-specific quenching. These results provide strong evidence that the strong and specific quenching (increase of k_{Yb_NR}, k_{NR2}, and k_{NR3}) in toluene is related to the aromatic =C–H stretching.

Further evidence for distinct quenching was obtained by performing the same experiments in cyclohexane (**Figure 3c**) because the aliphatic C–H stretching frequency is lower compared to the aromatic =C–H stretching in toluene and very similar to the aliphatic C–H stretching frequency of the oleate capping ligands (**Table 1**). The weaker relative increases of k_{NR2} (6, 48, and 68-fold for the 39 nm, 31 nm, and 27 nm c-UCNCs, respectively), and k_{NR3} (23, 26, and 31-fold for the 39 nm, 31 nm, and 27 nm c-UCNCs, respectively) (see **Supporting Table S3**) compared to toluene confirmed the specific quenching by the aromatic =C–H stretching in toluene. On the contrary, the strong increase of k_{NR5} (608, 2250, and 6410 fold for the 39 nm, 31 nm, and 27 nm c-UCNCs, respectively) in cyclohexane was most probably caused by a phonon-assisted coupling of the fundamental vibrational frequency of the aliphatic C–H stretching to the *5Er* → *4Er* transition, thus directly relaxing the red-emitting *5Er* level.[19,38] This result would suggest a stronger quenching of the red UCL. However, compared to toluene, the green/red UCL intensity ratio increases less with decreasing size (**Figure 4b**), suggesting that the relaxation of the non-radiative transitions in the lower lying Yb^{3+} and Er^{3+} states is the main contributor to UCL quenching. This result also highlights the robustness of our model toward perturbation and the non-linearity in response of the system to a stimulus, both characteristics of complex systems.[15,41]

Penetration depth of quenching effects from the solvent. NCs are characterized by a large surface-to-volume ratio that makes them more sensitive to the interaction with the surrounding environment. As a consequence, the Er^{3+} ions closer to the surface are more affected by solvent quenching and participate less in UC than the ones in the inner part of the UCNC, as confirmed by different studies.[19,25,29,30] Although these studies showed surface-distance-dependent quenching and a layer of ~4 nm was found to efficiently suppress UCL quenching,[30] existing macroscopic models do not provide spatial resolution because the UCNCs are modeled as one single and homogeneous entity.[20,21,24-26] However, such spatial resolution can become important because with decreasing UCNC size, the UCL quenching penetration zone takes a larger volume fraction of the overall UCNC and quenching becomes more significant. The lack of spatial resolution of common rate-equation models is a disadvantage for an accurate description

of UCL because it neglects (or considers infinitely rapid) the energy migration inside the UCNC.[14,43] Microscopic kinetic models can provide spatial resolution by considering the ET network between single ions inside the NCs.[15,23,27] However, they require multi-step processes to account for the complex energy level schemes of UCNCs. With the aim to account for the extent to which Er^{3+} ions close to the surface participate in UCL, we implemented a two-compartment approach that combines the advantages of both macroscopic and microscopic models. This advanced model can better describe the ET processes between the energetic transitions in the UCNC and the vibrational transitions of the quenchers (capping ligands and solvent molecules),[19] whose probability scales with the distance, and thus, determine the amount of Er^{3+} ions affected by quenching more accurately.

The two-compartment model considers each UCNC as being composed of an inner core zone and an outer layer zone. The initial populations of each electronic state of activators and sensitizers (*1Er*, *3Er*, *1Yb,* and *2Yb*) are divided according to the corresponding volume fractions. In another two-layer model proposed by Berry *et al.*,[22] the UCL contribution from the external layer was considered as negligible. However, this approximation is only acceptable for large UCNCs, in which the UCL quenching penetration zone presents a small volume fraction. Moreover, their approach considered only the energy migration between Yb^{3+} ions as possible communication channels between the two layers. Producing small UCNCs with high brightness is one of the most important challenges in UCNC research and models adapted to small UCNCs that can account for all possible ET pathways are paramount for their successful design. Our two-compartment model includes all possible pathways for ET between the two compartments, *i.e.*, energy migration between Yb^{3+} ions and ET, BET, and CR between Yb^{3+} and Er^{3+} and Er^{3+} and Er^{3+} ions in the different compartments, thereby providing spatial resolution of UCL quenching. The concept of the model, including the new processes and new terms to be considered, is summarized in **Figure 5** (for more details see Materials and Methods section). Each compartment can be described by a similar set of differential equations that was used for the single compartment approach and additional terms account for the communication channels between the two compartments.

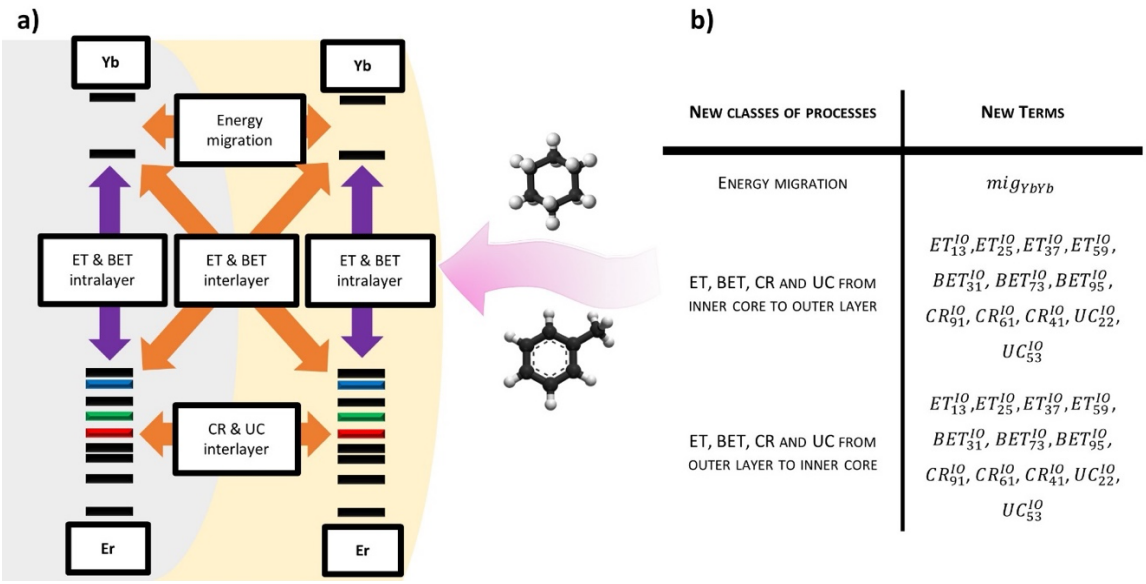

Figure 5. a) Schematic presentation of the two-compartment model concept. In addition to transitions occurring within either the inner core or the outer layer cross transitions are possible, involving bimolecular processes, one relative to the core and the other relative to the outer layer. Purple arrows represent intralayer transitions, whereas orange arrows represent interlayer transitions (energy migration, ET and BET, CR and UC). **b)** New types of processes in the two-compartment model and the respective terms that account for the communication between the inner core (I) and the outer layer (O).

To test the spatial resolution performance of the two-compartment model, we sought to determine the penetration depth of UCL quenching. To do so, we used the UCL kinetics of the 27 nm c-UCNCs in toluene and calculated the average of the four mainly changing non-radiative kinetic constants (k_{NR} = [$k_{Yb\_NR} + k_{NR2} + k_{NR3} + k_{NR5}$]/4) of the c-UCNCs divided into inner core and outer layer zones of different thicknesses (**Figure 6a**). In a 2 nm thick outer layer, k_{NR} was much higher than in the complete (single compartment) UCNC, which showed that a large fraction of the outer layer RE ions was quenched by the solvent. For the inner core (decreasing from 27 nm to 23 nm in diameter) k_{NR} decreased similarly to the volume fraction (relative decrease of ~40%), which represents the missing quenching that was outsourced to the outer layer. From 2 nm to 4 nm layer thickness, k_{NR} decreased for both inner core and outer layer, whereas it remained constant for thicker layers. This behavior provides good evidence that UCL quenching is strongest at the surface (decrease of k_{NR} in the outer layer with increasing thickness) but can still penetrate up to ~4 nm inside the UCNC (decrease of k_{NR} in the inner core with reduced volume). This result is consistent with previous reports, in which an inert shell of ~4 nm was found to well isolate the inner core from solvent quenching,[32,44–46] and confirms the excellent spatial resolution of our two-compartment model. To further investigate the solvent influence on the UCL penetration zone (*i.e.*, 4 nm outer layer) we also modeled the 27 nm c-UCNCs UCL in cyclohexane and deuterated toluene. In all the three different solvents the non-radiative constants change much stronger for the outer layer

compared to the inner core. Their values are also much higher than those calculated with the single-compartment approach (**Supporting Table S4**), where the quenching effect is averaged over the entire UCNC.

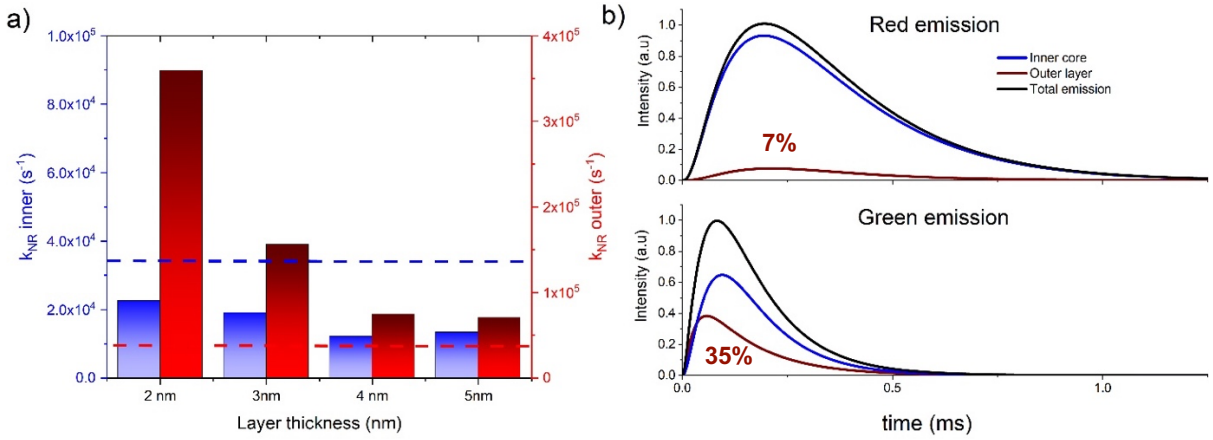

Figure 6. Application of the two-compartment model to 27 nm c-UCNCs in toluene: **a)** Average of primarily quenched non-radiative constants (k_{NR}) for the inner core (blue) and the outer layer (red) for different outer layer thicknesses. The dashed lines present the k_{NR} value without outer layer (single-compartment model). Please note that the outer layer ordinate values (red) are 4 times larger than the ones from the inner core ordinate (blue). **b)** Calculated contribution of inner core (blue) and outer layer (dark red) to the total red (top) and green (bottom) UCL emissions. Total intensity is normalized to the highest intensity value. Percent values present the relative contribution of the outer layer to the total UCL intensity.

Using the two-compartment approach, we were also able to determine the contributions of the two zones to red and green UCL (**Figure 6b**). Notably, the outer layer contribution to the overall UCL emission is not at all negligible for the relatively small UCNCs. In particular, for green emission, the outer layer contributed ~35% to the overall emission. Considering that the green UCL intensity is ~17-fold higher than the red one (**Figure 4b**), the outer layer strongly contributed to UCL in toluene despite the significant UCL quenching via the UCNC surface. The results also confirm the much stronger effect of solvent quenching on the red emission, for which the outer layer contribution is very small (~7%) compared to the inner core. The spatially resolved UCL contribution is also solvent-specific as shown by the differences in cyclohexane (outer layer contributions of 20% and 15% for red and green, respectively) and deuterated toluene (outer layer contributions of 25% for both red and green). In cyclohexane (**Supporting Figure S5a**), the outer layer red emission is significantly less quenched compared to toluene, which underlines the stronger effect of quenching on the lower energy states than on the emitting state (*5Er*), as already found in the single-compartment model (*vide supra*). The similar contributions of the outer layer (~25 %) and the inner core (~75%) to both red and green UCL in deuterated toluene (**Supporting Figure S5b**) confirm the non-specific and much weaker quenching via the =C–D stretching vibrational frequency. However, considering that the 4 nm outer layer volume

presents ~65% of the total c-UCNC volume, a significantly stronger UCL quenching of the outer layer (compared to the inner core) is obvious even in deuterated toluene.

A very interesting feature of the two-compartment model is the possibility of combining spatial resolution with the simulation of both rise and decay of the UCL to determine the different population dynamics of the inner core and the outer layer. Intuitively, one may expect that the increase of the non-radiative constants of the outer layer would lead to shorter UCL rise and/or decay times and a concomitant faster depopulation. However, the calculated population profiles of red (*5Er*) and green (*6Er*) emitting levels clearly show that the rise in the outer layer is significantly slower than the one in the inner core, which means that the maximum population of the inner core is reached before the one of the outer layer (**Figure 7**). This behavior can be attributed to two effects. First, the non-radiative relaxation of the low energy reservoir states of the outer layer is faster (due to the higher kinetic constants), such that the maximum population of the emitting states will be reached after longer times. Second, thanks to inter-layer energy migration, the inner core states can act as additional reservoirs for the outer layer to supply the excitation required for UCL. This second effect is not instantaneous, thus, the time required for the excitation to pass from one layer to the other in order to populate the outer emitting states is longer. Again, solvent-induced quenching plays an important role for the spatially resolved population dynamics. While the population profiles look quite similar in cyclohexane (apart from the generally longer rise and decay times in the aliphatic solvent, **Supporting Figure S6a**), the ones in deuterated toluene show the opposite, *i.e.*, the outer layer population is significantly faster (**Supporting Figure 6b**). Similar to the UCL contributions of the two zones, the non-specific and much weaker quenching in deuterated toluene is the most probable explanation of this opposite spatial population behavior. The depopulation contribution from quenching is smaller than in toluene or cyclohexane, whereas the population contributions from energy migration, ET, and CR are similar. These contributions are partial derivatives of the population curve and adding a less negative derivative (quenching) to a positive derivative (population), results in a steeper positive slope for both red- and green-emitting states populations.

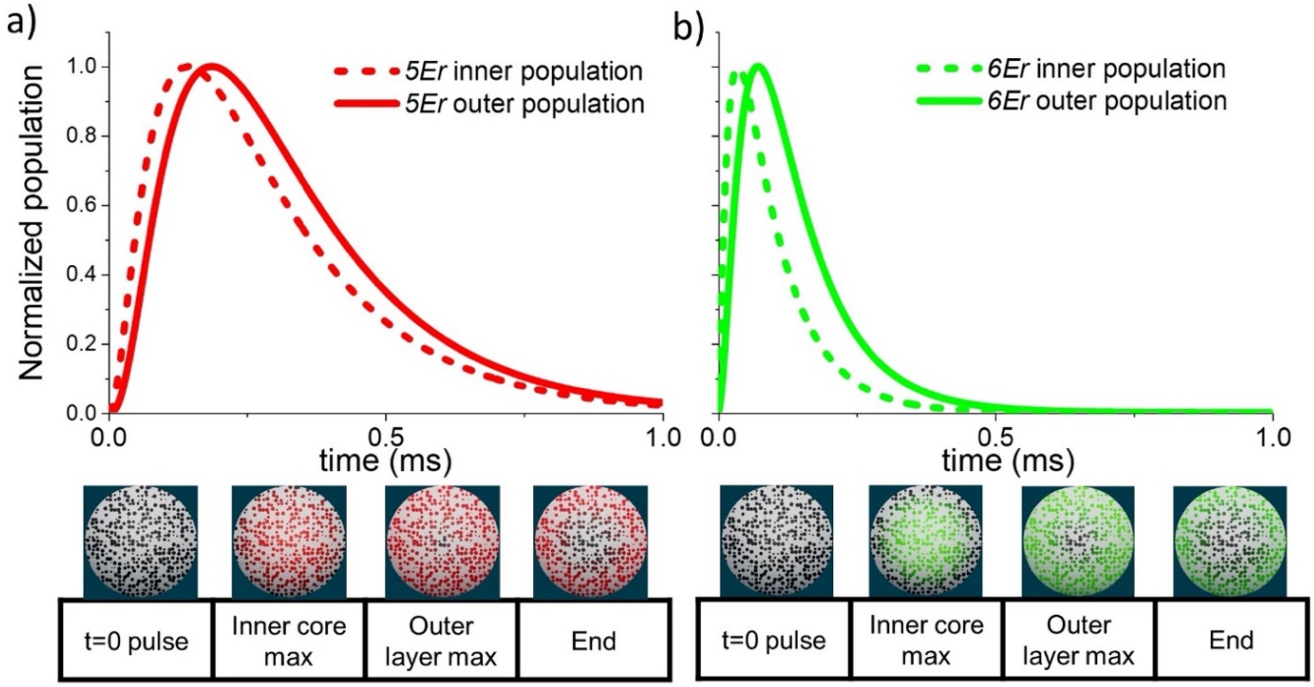

Figure 7. Normalized population profiles of the inner core and the outer layer for red (**a**) and green (**b**) emitting states over time. The bottom graphs represent the spatial distribution of the populated emitting states. Black color represents the absence of population while red or green color represents the population of *5Er* and *6Er*, respectively.

Conclusions

In summary, we have presented a detailed study on the UC dynamics of $NaYF_4$:Yb^{3+},Er^{3+}. We have analyzed the optical properties $NaYF_4$:Yb^{3+},Er^{3+} upon pulsed 980 nm excitation by a kinetic model developed with the freely accessible software COPASI. By systematically modelling UCNCs with different sizes ranging from 27 nm to 39 nm and dispersed in different non-polar solvents we could determine the main loss pathways competing with UCL and their dependence on solvent and UCNC size. The UCL kinetics could be very well modeled by our simpler *single-compartment* approach, which accounts for rise and decay kinetics and all population and depopulation pathways. Core-shell $NaYF_4$:Yb^{3+},Er^{3+}@$NaYF_4$ UCNCs with an inert shell thick enough (4 nm) to effectively shield the inner core from the surface-based quenching processes was used as a reference to estimate the bulk-like kinetic constants of each process. The obtained constants were then used as starting parameters to model the UCL kinetics of different c-UCNCs (27 nm, 31 nm, and 39 nm in diameter) in toluene, deuterated toluene, and cyclohexane, respectively. Out of the many energy pathways, our model efficiently identified four non-radiative relaxations as the most affected by quenching because of their resonance with the vibrational frequencies and overtones of solvent/ligand molecules interacting with the UCNC surface. In toluene, the main quencher was aromatic =C-H stretching, which produces a significant

increase in the depopulation rate of low-energy electronic states of both Yb^{3+} and Er^{3+} ions, with strong downstream effects on the radiative emission transitions. In particular, we have demonstrated that the depopulation of these low-energy states leads to a strong quenching of red emission because one of the two main pathways for populating the red emitting state of Er^{3+} becomes less favorable as the UCNC size decreases and consequently an increase of green/red intensity ratio is observed. These outcomes were further confirmed by strongly reduced quenching in deuterated toluene and by the poor resonance between the aliphatic C–H stretching modes of cyclohexane and the electronic transitions of the Er^{3+} ion.

A highly important feature of our kinetic model is the implementation of spatial resolution via a *two-compartment* approach. This aspect is particularly relevant for small UCNCs characterized by a high-surface-to-volume-ratio. Dividing the c-UCNC in an inner core and an outer layer, the model can account for all inter and intra-zone energy pathways as well as for interactions with the environment. The UCL quenching penetration depth could be determined as ~4 nm, which was in line with previous experimental studies that identified a 4 nm outer inert shell as the minimum thickness for suppressing surface related UCL quenching. The two-compartment model could also determine the contribution of the 4 nm thick UCL-quenching zone to the overall UCL with significant differences for the green and red emission and the different solvents. Despite the strong UCL quenching of toluene via the UCNC surface, the contribution of the outer layer to green UCL was 35% with a green-to-red intensity ratio of 17, which demonstrated the very significant contribution of surface-near RE ions to UCL in small UCNCs. Increased contributions of the outer layer to the red UCL in cyclohexane and deuterated toluene confirmed the weaker surface quenching in those solvents. Finally, our two-compartment model could determine the solvent-dependent population and depopulation dynamics of RE states with both spatial and temporal resolution. While the outer layer population of red and green emitting states was slower (compared to the inner core) in toluene and cyclohexane, it was the opposite in deuterated toluene.

Overall, our approach can precisely model both rise and decay UCL kinetics and provide important qualitative and quantitative information concerning solvent and size specific quenching of kinetic constants. The spatial and temporal resolution included in our two-compartment model allows for a closer look inside the UCL dynamics, which is of particular interest for optimizing small UCNCs (below ~40 nm), for which the outer layers can significantly contribute to UCL despite the large surface-to-volume ratios and the strong surface quenching. We believe that our versatile kinetic model developed with an easily accessible stand-alone program (COPASI) will become a very useful tool to researchers, who seek to design and optimize UCNCs for various applications. The model, developed for the prototypical oleate-capped $NaYF_4$:Yb^{3+},Er^{3+} UCNCs dispersed in organic solvents, can be easily

extended to more complex systems, including UCNCs doped with other RE ions (*e.g.*, Nd^{3+}, Tm^{3+}), smaller and multi-shell UCNCs (or other UCNC architectures), UCNCs coated with different hydrophilic ligands and dispersed in aqueous media, and UCNCs functionalized with biomolecules for Förster resonance ET (FRET) or other ET-based applications.

Experimental Section

Materials. Yttrium (III) oxide, (99.9%), ytterbium (III) oxide, (99.9%), and erbium (III) oxide, (99.99%) were purchased from Alfa Aesar. Hydrochloric acid (37%), sodium trifluoroacetate (98%), ammonium fluoride (98%), sodium hydroxide (97%), 1-octadecene (ODE, 90%), oleic acid (OA, 90%), oleylamine (OM, 97%), ethanol (EtOH, 99.8%), toluene (99.9%), deuterated toluene (99%), and trifluoroacetic acid (99%) were purchased from Sigma-Aldrich. Methanol (99.9%) was purchased from Romil Pure Chemistry. *n*-Hexane (97%) was purchased from VWR Chemicals. Cyclohexane (99%) was purchased from Acros Organics. All chemicals were used as received without further purifications. Highly pure water (Millipore) of resistivity greater than 18.0 MΩ cm was used in all experiments.

Synthesis of oleate-capped β-$NaYF_4$:Yb^{3+}(20%), Er^{3+}(2%) nanocrystals (c-UCNCs). The synthesis of β-$NaYF_4$:Yb^{3+}(20%),Er^{3+}(2%) UCNCs was carried out by a modified literature procedure.[10] RE chloride precursors were prepared from the RE oxides. Briefly, Y_2O_3 (0.78 mmol), Yb_2O_3 (0.20 mmol), and Er_2O_3 (0.02 mmol) were dissolved in 4.2 mL of 1.7 M HCl aqueous solution in a three-neck round bottom flask. The solution was stirred under reflux at 80 °C until the solution became clear. Then, the solvent was slowly evaporated at 65 °C. The powder was dried further in the oven at 105 °C overnight. Upon removal from the oven, 6 mL of OA and 15 mL of ODE were added to the flask containing the above prepared RE chloride precursors. The mixture was heated to 150 °C under vacuum and magnetic stirring until the precursors were completely dissolved and then cooled down to room temperature under argon flow. A solution of NaOH (2.5 mmol) and NHF_4 (4.0 mmol) in methanol (10 mL) was added drop by drop in the flask. Subsequently, the solution was slowly heated under argon flow and magnetic stirring until 120 °C to remove the methanol and then heated to 300 °C and kept at this temperature for 70 min. Then the solution was cooled down to room temperature under argon flow and the NCs were precipitated from the solution with ethanol (~40 ml) and collected by centrifugation (2147 RCF for 15 min). The resulting white pellet was further washed four times with a mixture of hexane/ethanol (1/3) and isolated by centrifugation (2147 RCF, 15 min). Finally, the white pellet was stored in ethanol. A small amount of powder was dried for XRD, DRIFT, and TGA analysis.

Synthesis of β-$NaYF_4$ sacrificial nanocrystals (s-NCs). β-$NaYF_4$ sacrificial NCs were synthesized via the co-thermolysis of sodium and yttrium trifluoroacetate using a previously reported procedure.[10] The $Y(CF_3COO)_3$ precursor was prepared by mixing Y_2O_3 (2 mmol) with 5 mL of ultrapure water and 5 mL of trifluoroacetic acid (TFA) in a three-necks bottom round flask and refluxing under stirring at 80°C overnight. Hereafter, the excess of water and TFA were slowly removed by evaporation in air at 65 °C. The obtained solid was further dried in the oven at 105 °C overnight. Upon removal from oven, 2 mmol of sodium trifluoroacetate (NaTFA) was added to the precursors' flask along with 6 mL of OA, 6 mL of OM, and 10 mL of ODE under argon flow. First, the mixture was heated to 125 °C under vacuum and vigorous stirring for several minutes to remove oxygen and residual water and successively to 290 °C under argon flow and kept at this temperature for 45 min. The light-yellow turbid solution obtained was cooled to room temperature and the s-NCs were precipitated by adding ethanol and isolated by centrifugation (2147 RCF, 15 min). The obtained precipitate was washed twice as reported for c-UCNCs. Finally, the nanocrystals were dispersed in ODE (0.3 mM).

Synthesis of oleate-capped β-$NaYF_4$:Yb^{3+}(20%),Er^{3+}(2%)/$NaYF_4$ nanocrystals (cs-UCNCs). The synthesis of cs-UCNCs was based on a previously described protocol.[10] First, the β-$NaYF_4$:Yb^{3+}(20%), Er^{3+}(2%) core was synthesized as previously described above for c-UCNCs. After heating the reaction mixture at 300 °C for 70 min, 1 mL aliquot was collected. Immediately after that, 1 mL of α-$NaYF_4$ dispersion in ODE (0.3 mM) was injected in one shot. The mixture was ripened at 300 °C for 15 min to allow the growth of the $NaYF_4$ shell around the core NCs. In order to obtain a thicker inert shell, after 15 min, 1.0 mL of the reaction mixture was collected (sample with a thin shell), and immediately after again 1 mL of α-$NaYF_4$ dispersion in ODE (0.3 mM) s-NCs were injected. The mixture was ripened for another 15 min to yield core-shell-shell NCs. Then the solution was cooled down to room temperature and the cs-UCNCs were precipitated by addition of ethanol and centrifugation (2147 RCF, 15 min). The white precipitate was washed as described for c-UCNCs. Finally, NCs were stored under ethanol.

Transmission Electron Microscopy (TEM). TEM grids were prepared by drop-casting (~50 μL) of oleate-capped UCNCs dispersion in toluene (1 mg/mL^{-1}) onto 400-mesh carbon-coated Cu grids, followed by air-drying. Electron microscopy images were taken on a FEI Tecnai G2 TEM operating at 100 kV, equipped with an Olympus Veleta camera. The Fiji ImageJ software was used to determine the UCNCs size, which was obtained as the average diameter of 200 individual NCs (**Figure 1a** for c-UCNCs and cs-UCNCs and **Supporting Figure S1a** for s-NCs). Each intermediate of the core–shell sample was analysed in order to determine the shell thickness.

Powder X-ray Diffraction (PXRD). PXRD measurements were carried out with a Bruker D8 Advance diffractometer using Cu Kα radiation (λ = 1.5406 Å) at a voltage of 40 kV and current of 40 mA. PXRD patterns (**Figure 1b** for c-UCNCs and cs-UCNCs and **Supporting Figure S1b** for s-NCs) were collected for 2θ = 10–70°, with a step size of 0.03° and a counting time of 10 s per step. The crystalline phases were identified by the search-match method using the JCPDS database.

Diffuse Reflectance Infrared Fourier Spectroscopy (DRIFT). DRIFT spectra were obtained employing a Bruker IFS 66 spectrometer working in diffuse reflectance mode and displayed in Kubelka-Munk units.[47] The resolution of the spectra was 4 cm^{-1}. Samples were diluted with KBr before measurement. KBr was used to collect the background. The bands at 2920, 2848, 1548, and 1452 cm^{-1} (**Supporting Figure S2a**), characteristic of asymmetric and symmetric C-H and O=C–O stretching modes of surface-bound oleates, confirmed the presence of an oleate capping layer on the surface of the UCNCs.

Thermal Gravimetric Analysis (TGA). TGA was carried out under nitrogen atmosphere using the SDT 2960 Simultaneous DSC-TGA system (TA Instruments). Thermograms were collected from RT to 700 °C at 10 °C min^{-1} heating rates under nitrogen flow. The weight loss observed at ∼450 °C was ∼33% for s-NCs, 12% for c-UCNCs, and 11% for cs-UCNCs (**Supporting Figure S2b**). The lower amount of organic capping layer for c-UCNCs and cs-UCNCs agrees with the higher surface-to-volume ratio of the s-NCs.

UCL measurements. Steady-state emission spectra were measured on Fluorolog FL3-21 (Horiba Scientific) equipped with a 5 W / 980 nm laser (Changchun New Industries). Samples had a concentration of 5 mg/mL and were measured in 2 mm quartz cuvettes (Starna) in the 350-750 nm range with a power density of 1.23 W cm^{-2}, an emission slit width of 1 nm and a step size of 1 nm. Time-resolved measurements were performed using a fluorescence plate reader (Edinburgh Instruments) equipped with a 2 W / 980 nm (Changchun New Industries) and a PM-1 laser modulation box (Edinburgh Instruments) to control the temporal parameters of the excitation pulse. Excitation and emission were separated using a 900 nm dichroic mirror (Edmund Optics). The signals were measured with a photomultiplier tube (PMT) by using 542/20 nm and 660/13 nm bandpass filters (Semrock) for the green and red emission, respectively. 150 µL of a UCNC dispersions (1 mg/mL) in toluene, deuterated toluene, or cyclohexane, were pipetted into 96-well glass-coated microplates (Thermo Fisher). The measurements were performed with a power density of 12.3 $mW \cdot cm^{-2}$ per pulse and a repetition rate of 200 Hz. All measurements were done in triplicates.

Kinetic modelling. Two different kinetic models were used to analyse the photophysical processes occurring inside the UCNCs. The first and simpler one, named *single-compartment* kinetic model as the one firstly proposed by Berry *et al*.,[20,22] describes the energy distribution in the different electronic states of Yb^{3+} and Er^{3+} ions following NIR excitation. It considers the whole UCNC as a single compartment with a homogeneous behaviour. It takes into account all the different elementary photophysical processes (**Figure 2**) including direct light absorption, self-absorption, ET, CR, UC, and radiative (R) and non-radiative (NR) relaxation.[48–50] The rate of change in population for each electronic states is described by a differential equation (more details can be found in the Supporting Information) with the time evolution as the sum of the population and the depopulation terms.[51] These terms, which are proportional to the concentration of the species participating in the elementary process, can be distinguished as "monomolecular" or "bimolecular" on the base of the number of ions involved. The solution of the system of equations was numerically obtained by using the COPASI software.[31] A summary of the processes and of the relative kinetic equations is provided in the Supporting Information.

A second and more accurate model, named *two-compartment* kinetic model, was developed to evaluate the penetration depth of quenching effects by the environment into the UCNC. Briefly, it considers the UCNC consisting of two compartments: an inner core and an outer layer. While the inner core does not interact directly with the environment, it can only be affected by the NC outer layer, the same cannot be said for the outer layer. Besides interacting with the inner core, the outer layer directly interacts with the environment, such that the RE ions are more affected by it. Therefore, each layer was considered as a single compartment, and then modelled as previously introduced for the single-compartment model using the kinetic constants found for the core-shell system as starting values. The only difference was that while in the inner core they were all fixed except the non-radiative ones, in the outer layer all the kinetic constants were left free to change. In addition, the energy migrations (exchanges) between the inner core (*I*) and the outer layer (*O*) were considered as schematized in **Figure 5**.

Specifically, the following inter-layer transitions were considered: energy migration between Yb^{3+} ions in different layers (Equation 3); ET from Yb^{3+} to Er^{3+} ions, (Equation 4); BET from Er^{3+} to Yb^{3+} ions (Equation 5); CR between Er^{3+} ions (Equation 6); and UC between Er^{3+} ions (Equation 7).

$$\left(\frac{\partial n_{2Yb}^{I}}{\partial t}\right)_{mig} = -k_{mig} n_{2Yb}^{I} n_{1Yb}^{O} \qquad (3)$$

$$\left(\frac{\partial n_{2Yb}^{I}}{\partial t}\right)_{ETij^{IO}} = -k_{ETij}^{IO} n_{2Yb}^{I} n_{iEr}^{O} \quad (4)$$

$$\left(\frac{\partial n_{2Yb}^{I}}{\partial t}\right)_{ETij^{IO}} = k_{ETij}^{IO} n_{1Yb}^{I} n_{iEr}^{O} \quad (5)$$

$$\left(\frac{\partial n_{iEr}^{I}}{\partial t}\right)_{CRhk^{IO}} = k_{CRhk}^{IO} n_{hEr}^{I} n_{kEr}^{O} \quad (6)$$

$$\left(\frac{\partial n_{iEr}^{I}}{\partial t}\right)_{UChk^{IO}} = k_{UChk}^{IO} n_{hEr}^{I} n_{kEr}^{O} \quad (7)$$

Equations 3-6 account for excitations from both the inner core to the outer layer (IO) and from the outer layer to the inner core (OI). All these constants were left free to change during the simulation. In order to better assess the extent to which Er^{3+} ions close to surface participate to UC, outer layers of varying thickness were considered.

Supporting Information

Set of differential equations used for the single compartment kinetic model; TEM and PXRD data of s-UCNCs; UCL spectra of cs- and c-UCNCs in cyclohexane and deuterated toluene; DRIFT and thermogravimetric data of oleates, s-UCNCs, c-UCNCs, and cs-UCNCs; experimental and simulated time-resolved green and red emission of cs-UCNCs; UCL contributions of inner core and outer layer in cyclohexane and deuterated toluene; normalized population profiles in cyclohexane and deuterated toluene; kinetic constants for cs-UCNCs and c-UCNCs in toluene; kinetic constants for cs-UCNCs and c-UCNCs in deuterated toluene; kinetic constants for cs-UCNCs and c-UCNCs in cyclohexane; comparison of non-radiative kinetic constants of single and two-compartment models.

Acknowledgements

This work has been financed by Université Franco-Italienne (UFI, PhD fellowship of Federico Pini), the European Commission (Marie Skłodowska-Curie grant 794410), Université Rouen Normandie, INSA Rouen Normandie, Centre National de la Recherche Scientifique, the European Regional Development Fund, Labex SynOrg (ANR-11-LABX-0029), Carnot Institute I2C, XL-Chem graduate school (ANR-18-EURE-0020 XL CHEM), Région Normandie, the Korean National Research Foundation, Université Paris-Saclay, Seoul National University, Istituto di Chimica della Materia Condensata e Tecnologie dell'Energia, Consiglio Nazionale delle Ricerche, program of scientific cooperation CNR/CAS 2019-2021, and the ERASMUS+ traineeship programme of University of Padova. Dr. F. Boldrin and Dr. F. Caicci (Department of Biology, University of Padova) are acknowledged for producing TEM images.

References

(1) Heer, S.; Kömpe, K.; Güdel, H.-U.; Haase, M. Highly Efficient Multicolour Upconversion Emission in Transparent Colloids of Lanthanide-Doped NaYF4 Nanocrystals. *Adv. Mater.* **2004**, *16* (23–24), 2102–2105. https://doi.org/10.1002/adma.200400772

(2) Heer, S.; Lehmann, O.; Haase, M.; Güdel, H.-U. Blue, Green, and Red Upconversion Emission from Lanthanide-Doped $LuPO_4$ and $YbPO_4$ Nanocrystals in a Transparent Colloidal Solution. *Angew. Chem. Int. Ed.* **2003**, *42* (27), 3179–3182. https://doi.org/10.1002/anie.200351091

(3) Auzel, F. Upconversion and Anti-Stokes Processes with f and d Ions in Solids. *Chem. Rev.* **2004**, *104* (1), 139–174. https://doi.org/10.1021/cr020357g

(4) Boyer, J.-C.; Manseau, M.-P.; Murray, J. I.; van Veggel, F. C. J. M. Surface Modification of Upconverting $NaYF_4$ Nanoparticles with PEG−Phosphate Ligands for NIR (800 Nm) Biolabeling within the Biological Window. *Langmuir* **2010**, *26* (2), 1157–1164. https://doi.org/10.1021/la902260j

(5) Haase, M.; Schäfer, H. Upconverting Nanoparticles. *Angew. Chem. Int. Ed.* **2011**, *50* (26), 5808–5829. https://doi.org/10.1002/anie.201005159

(6) Gnach, A.; Lipinski, T.; Bednarkiewicz, A.; Rybka, J.; Capobianco, J. A. Upconverting Nanoparticles: Assessing the Toxicity. *Chem. Soc. Rev.* **2015**, *44* (6), 1561–1584. https://doi.org/10.1039/C4CS00177J

(7) Francés-Soriano, L.; Peruffo, N.; Natile, M. M.; Hildebrandt, N. Er^{3+}-to-Dye Energy Transfer in DNA-Coated Core and Core/Shell/Shell Upconverting Nanoparticles with 980 Nm and 808 Nm Excitation of Yb^{3+} and Nd^{3+} *Analyst* **2020**, *145* (7), 2543–2553. https://doi.org/10.1039/C9AN02532D

(8) Algar, W. R.; Hildebrandt, N.; Vogel, S. S.; Medintz, I. L. FRET as a Biomolecular Research Tool — Understanding Its Potential While Avoiding Pitfalls. *Nat. Methods* **2019**, *16* (9), 815–829. https://doi.org/10.1038/s41592-019-0530-8

(9) Meijer, M. S.; Talens, V. S.; Hilbers, M. F.; Kieltyka, R. E.; Brouwer, A. M.; Natile, M. M.; Bonnet, S. NIR-Light-Driven Generation of Reactive Oxygen Species Using Ru(II)-Decorated Lipid-Encapsulated Upconverting Nanoparticles. *Langmuir* **2019**, *35* (37), 12079–12090. https://doi.org/10.1021/acs.langmuir.9b01318

(10) Meijer, M. S.; Natile, M. M.; Bonnet, S. 796 Nm Activation of a Photocleavable Ruthenium(II) Complex Conjugated to an Upconverting Nanoparticle through Two Phosphonate Groups. *Inorg. Chem.* **2020**, *59* (20), 14807–14818. https://doi.org/10.1021/acs.inorgchem.0c00043

(11) Nsubuga, A.; Sgarzi, M.; Zarschler, K.; Kubeil, M.; Hübner, R.; Steudtner, R.; Graham, B.; Joshi, T.; Stephan, H. Facile Preparation of Multifunctionalisable 'Stealth' Upconverting Nanoparticles for Biomedical Applications. *Dalton Trans.* **2018**, *47* (26), 8595–8604. https://doi.org/10.1039/C8DT00241J

(12) Ximendes, E. C.; Santos, W. Q.; Rocha, U.; Kagola, U. K.; Sanz-Rodríguez, F.; Fernández, N.; Gouveia-Neto, A. da S.; Bravo, D.; Domingo, A. M.; del Rosal, B.; Brites, C. D. S.; Carlos, L. D.; Jaque, D.; Jacinto, C. Unveiling in Vivo Subcutaneous Thermal Dynamics by Infrared Luminescent Nanothermometers. *Nano Lett.* **2016**, *16* (3), 1695–1703. https://doi.org/10.1021/acs.nanolett.5b04611

(13) Tessitore, G.; Mandl, G. A.; Brik, M. G.; Park, W.; Capobianco, J. A. Recent Insights into Upconverting Nanoparticles: Spectroscopy, Modeling, and Routes to Improved Luminescence. *Nanoscale* **2019**, *11* (25), 12015–12029. https://doi.org/10.1039/C9NR02291K

(14) Agazzi, L.; Wörhoff, K.; Pollnau, M. Energy-Transfer-Upconversion Models, Their Applicability and Breakdown in the Presence of Spectroscopically Distinct Ion Classes: A Case Study in Amorphous Al_2O_3:Er^{3+}. *J. Phys. Chem. C* **2013**, *117* (13), 6759–6776. https://doi.org/10.1021/jp4011839

(15) Teitelboim, A.; Tian, B.; Garfield, D. J.; Fernandez-Bravo, A.; Gotlin, A. C.; Schuck, P. J.; Cohen, B. E.; Chan, E. M. Energy Transfer Networks within Upconverting Nanoparticles Are Complex Systems with Collective, Robust, and History-Dependent Dynamics. *J. Phys. Chem. C* **2019**, *123* (4), 2678–2689. https://doi.org/10.1021/acs.jpcc.9b00161

(16) Liu, D.; Xu, X.; Du, Y.; Qin, X.; Zhang, Y.; Ma, C.; Wen, S.; Ren, W.; Goldys, E. M.; Piper, J. A.; Dou, S.; Liu, X.; Jin, D. Three-Dimensional Controlled Growth of Monodisperse Sub-50 Nm Heterogeneous Nanocrystals. *Nat. Commun.* **2016**, *7* (1), 10254. https://doi.org/10.1038/ncomms10254

(17) Liu, G. Advances in the Theoretical Understanding of Photon Upconversion in Rare-Earth Activated Nanophosphors. *Chem. Soc. Rev.* **2015**, *44* (6), 1635–1652. https://doi.org/10.1039/C4CS00187G

(18) Inokuti, M.; Hirayama, F. Influence of Energy Transfer by the Exchange Mechanism on Donor Luminescence. *J. Chem. Phys.* **1965**, *43* (6), 1978–1989. https://doi.org/10.1063/1.1697063

(19) Rabouw, F. T.; Prins, P. T.; Villanueva-Delgado, P.; Castelijns, M.; Geitenbeek, R. G.; Meijerink, A. Quenching Pathways in $NaYF_4$:Er^{3+},Yb^{3+} Upconversion Nanocrystals. *ACS Nano* **2018**, *12* (5), 4812–4823. https://doi.org/10.1021/acsnano.8b01545

(20) Anderson, R. B.; Smith, S. J.; May, P. S.; Berry, M. T. Revisiting the NIR-to-Visible Upconversion Mechanism in β-$NaYF_4$:Yb^{3+},Er^{3+} . *J. Phys. Chem. Lett.* **2014**, *5* (1), 36–42. https://doi.org/10.1021/jz402366r

(21) Zhao, J.; Lu, Z.; Yin, Y.; McRae, C.; Piper, J. A.; Dawes, J. M.; Jin, D.; Goldys, E. M. Upconversion Luminescence with Tunable Lifetime in $NaYF_4$:Yb,Er Nanocrystals: Role of Nanocrystal Size. *Nanoscale* **2013**, *5* (3), 944–952. https://doi.org/10.1039/C2NR32482B

(22) Hossan, M. Y.; Hor, A.; Luu, Q.; Smith, S. J.; May, P. S.; Berry, M. T. Explaining the Nanoscale Effect in the Upconversion Dynamics of β-$NaYF_4$:Yb^{3+} , Er^{3+} Core and Core–Shell Nanocrystals. *J. Phys. Chem. C* **2017**, *121* (30), 16592–16606. https://doi.org/10.1021/acs.jpcc.7b04567

(23) Villanueva-Delgado, P.; Krämer, K. W.; Valiente, R. Simulating Energy Transfer and Upconversion in β-$NaYF_4$: Yb^{3+}, Tm^{3+}. *J. Phys. Chem. C* **2015**, *119* (41), 23648–23657. https://doi.org/10.1021/acs.jpcc.5b06770

(24) Villanueva-Delgado, P.; Krämer, K. W.; Valiente, R.; Jong, M. de; Meijerink, A. Modeling Blue to UV Upconversion in β-$NaYF_4$:Tm^{3+}. *Phys. Chem. Chem. Phys.* **2016**, *18* (39), 27396–27404. https://doi.org/10.1039/C6CP04347J

(25) Frenzel, F.; Würth, C.; Dukhno, O.; Przybilla, F.; Wiesholler, L. M.; Muhr, V.; Hirsch, T.; Mély, Y.; Resch-Genger, U. Multiband Emission from Single β-$NaYF_4$(Yb,Er) Nanoparticles at High Excitation Power Densities and Comparison to Ensemble Studies. *Nano Res.* **2021**. https://doi.org/10.1007/s12274-021-3350-y

(26) Kong, J.; Shang, X.; Zheng, W.; Chen, X.; Tu, D.; Wang, M.; Song, J.; Qu, J. Revisiting the Luminescence Decay Kinetics of Energy Transfer Upconversion. *J. Phys. Chem. Lett.* **2020**, *11* (9), 3672–3680. https://doi.org/10.1021/acs.jpclett.0c00619

(27) Baride, A.; May, P. S.; Berry, M. T. Cross-Relaxation from Er^{3+}($^2H_{11/2}$,$^4S_{3/2}$) and Er^{3+}($^2H_{9/2}$) in β-$NaYF_4$:Yb,Er and Implications for Modeling Upconversion Dynamics. *J. Phys. Chem. C* **2020**, *124* (3), 2193–2201. https://doi.org/10.1021/acs.jpcc.9b10163

(28) Tian, C.; Chen, X.; Shuibao, Y. Concentration Dependence of Spectroscopic Properties and Energy Transfer Analysis in Nd^{3+} Doped Bismuth Silicate Glasses. *Solid State Sci.* **2015**, *48*, 171–176. https://doi.org/10.1016/j.solidstatesciences.2015.08.008

(29) Kraft, M.; Würth, C.; Muhr, V.; Hirsch, T.; Resch-Genger, U. Particle-Size-Dependent Upconversion Luminescence of $NaYF_4$: Yb, Er Nanoparticles in Organic Solvents and Water at Different Excitation Power Densities. *Nano Res.* **2018**, *11* (12), 6360–6374. https://doi.org/10.1007/s12274-018-2159-9

(30) Fischer, S.; Bronstein, N. D.; Swabeck, J. K.; Chan, E. M.; Alivisatos, A. P. Precise Tuning of Surface Quenching for Luminescence Enhancement in Core–Shell Lanthanide-Doped Nanocrystals. *Nano Lett.* **2016**, *16* (11), 7241–7247. https://doi.org/10.1021/acs.nanolett.6b03683

(31) Hoops, S.; Sahle, S.; Gauges, R.; Lee, C.; Pahle, J.; Simus, N.; Singhal, M.; Xu, L.; Mendes, P.; Kummer, U. COPASI—a COmplex PAthway SImulator. *Bioinformatics* **2006**, *22* (24), 3067–3074. https://doi.org/10.1093/bioinformatics/btl485

(32) Bhuckory, S.; Hemmer, E.; Wu, Y.-T.; Yahia-Ammar, A.; Vetrone, F.; Hildebrandt, N. Core or Shell? Er^{3+} FRET Donors in Upconversion Nanoparticles. *Eur. J. Inorg. Chem.* **2017**, *2017* (44), 5186–5195. https://doi.org/10.1002/ejic.201700904

(33) Berry, M. T.; May, P. S. Disputed Mechanism for NIR-to-Red Upconversion Luminescence in $NaYF_4$:Yb^{3+},Er^{3+}. *J. Phys. Chem. A* **2015**, *119* (38), 9805–9811. https://doi.org/10.1021/acs.jpca.5b08324

(34) Rabouw, F. T.; den Hartog, S. A.; Senden, T.; Meijerink, A. Photonic Effects on the Förster Resonance Energy Transfer Efficiency. *Nat. Commun.* **2014**, *5* (1), 3610. https://doi.org/10.1038/ncomms4610

(35) Senden, T.; Rabouw, F. T.; Meijerink, A. Photonic Effects on the Radiative Decay Rate and Luminescence Quantum Yield of Doped Nanocrystals. *ACS Nano* **2015**, *9* (2), 1801–1808. https://doi.org/10.1021/nn506715t

(36) Sokolov, V. I.; Zvyagin, A. V.; Igumnov, S. M.; Molchanova, S. I.; Nazarov, M. M.; Nechaev, A. V.; Savelyev, A. G.; Tyutyunov, A. A.; Khaydukov, E. V.; Panchenko, V. Ya. Determination of the Refractive Index of β-$NaYF_4$/Yb^{3+}/Er^{3+}/Tm^{3+} Nanocrystals Using Spectroscopic Refractometry. *Opt. Spectrosc.* **2015**, *118* (4), 609–613. https://doi.org/10.1134/S0030400X15040190

(37) Fischer, S.; Hallermann, F.; Eichelkraut, T.; Plessen, G. von; Krämer, K. W.; Biner, D.; Steinkemper, H.; Hermle, M.; Goldschmidt, J. C. Plasmon Enhanced Upconversion Luminescence near Gold Nanoparticles–Simulation and Analysis of the Interactions. *Opt. Express* **2012**, *20* (1), 271–282. https://doi.org/10.1364/OE.20.000271

(38) Ramsay, D. A.; Sutherland, G. B. B. M.; Rideal, E. K. The Vibration Spectrum and Molecular Configuration of Cyclohexane. *Proc. R. Soc. Lond. Ser. Math. Phys. Sci.* **1947**, *190* (1021), 245–256. https://doi.org/10.1098/rspa.1947.0074

(39) Renero-Lecuna, C.; Martín-Rodríguez, R.; Valiente, R.; González, J.; Rodríguez, F.; Krämer, K. W.; Güdel, H. U. Origin of the High Upconversion Green Luminescence Efficiency in β-$NaYF_4$:2%Er^{3+},20%Yb^{3+}. *Chem. Mater.* **2011**, *23* (15), 3442–3448. https://doi.org/10.1021/cm2004227

(40) Appendix E: List of Common Vibrational Group Frequencies (Cm^{-1}). In *Modern Vibrational Spectroscopy and Micro-Spectroscopy*; John Wiley & Sons, Ltd, 2015; pp 397–398. https://doi.org/10.1002/9781118824924.app5

(41) Naruse, M.; Aono, M.; Kim, S.-J.; Kawazoe, T.; Nomura, W.; Hori, H.; Hara, M.; Ohtsu, M. Spatiotemporal Dynamics in Optical Energy Transfer on the Nanoscale and Its Application to Constraint Satisfaction Problems. *Phys. Rev. B* **2012**, *86* (12), 125407. https://doi.org/10.1103/PhysRevB.86.125407

(42) Zhang, Y.; Yu, Z.; Li, J.; Ao, Y.; Xue, J.; Zeng, Z.; Yang, X.; Tan, T. T. Y. Ultrasmall-Superbright Neodymium-Upconversion Nanoparticles via Energy Migration Manipulation and Lattice Modification: 808 Nm-Activated Drug Release. *ACS Nano* **2017**, *11* (3), 2846–2857. https://doi.org/10.1021/acsnano.6b07958

(43) Wang, F.; Wang, J.; Liu, X. Direct Evidence of a Surface Quenching Effect on Size-Dependent Luminescence of Upconversion Nanoparticles. *Angew. Chem. Int. Ed.* **2010**, *49* (41), 7456–7460. https://doi.org/10.1002/anie.201003959

(44) Rinkel, T.; Raj, A. N.; Dühnen, S.; Haase, M. Synthesis of 10 Nm β-$NaYF_4$:Yb,Er/$NaYF_4$ Core/Shell Upconversion Nanocrystals with 5 Nm Particle Cores. *Angew. Chem. Int. Ed.* **2016**, *55* (3), 1164–1167. https://doi.org/10.1002/anie.201508838

(45) Hyppänen, I.; Höysniemi, N.; Arppe, R.; Schäferling, M.; Soukka, T. Environmental Impact on the Excitation Path of the Red Upconversion Emission of Nanocrystalline $NaYF_4$:Yb^{3+},Er^{3+}. *J. Phys. Chem. C* **2017**, *121* (12), 6924–6929. https://doi.org/10.1021/acs.jpcc.7b01019

(46) Kortüm, G. *Reflectance Spectroscopy: Principles, Methods, Applications*; Springer-Verlag: Berlin Heidelberg, 1969. https://doi.org/10.1007/978-3-642-88071-1

(47) Judd, B. R. Optical Absorption Intensities of Rare-Earth Ions. *Phys. Rev.* **1962**, *127* (3), 750–761. https://doi.org/10.1103/PhysRev.127.750

(48) Ofelt, G. S. Intensities of Crystal Spectra of Rare-Earth Ions. *J. Chem. Phys.* **1962**, *37* (3), 511–520. https://doi.org/10.1063/1.1701366

(49) Kushida, T. Energy Transfer and Cooperative Optical Transitions in Rare-Earth Doped Inorganic Materials. I. Transition Probability Calculation. *J. Phys. Soc. Jpn.* **1973**, *34* (5), 1318–1326. https://doi.org/10.1143/JPSJ.34.1318

(50) Gillespie, D. T. Exact Stochastic Simulation of Coupled Chemical Reactions. *J. Phys. Chem.* **1977**, *81* (25), 2340–2361. https://doi.org/10.1021/j100540a008

TOC image